Hydrodynamic forces on a side-by-side ellipse pair with and without relative motion

Flow (2024), **4** E27
doi:10.1017/flo.2024.21

FLOW CAMBRIDGE UNIVERSITY PRESS

RESEARCH ARTICLE

Hydrodynamic forces on a side-by-side ellipse pair with and without relative motion

Preston Rhodes[1] and Wim M. van Rees[1,*]

[1]Department of Mechanical Engineering, Massachusetts Institute of Technology, Cambridge MA 02139, USA
*Corresponding author. E-mail: wvanrees@mit.edu

Received: 28 November 2023; **Revised:** 17 June 2024; **Accepted:** 24 June 2024

Keywords: Fluid-structure interactions; Underwater vehicles; Formation swimming; Hydrodynamic forces

Abstract

Motivated by flow interactions in schooling biological swimmers as well as in unmanned underwater vehicle fleets, we investigate the flow past two identical 6 : 1 ellipses using two-dimensional simulations at Reynolds numbers of $O(10^3)$. When both ellipses move at the same velocity, overall drag reductions of 10 %–20 % can be achieved in staggered formations, with the strongest drag reductions occurring at the smallest lateral distances. In side-by-side configurations, the drag on both bodies increases by 10 %–20 %. Lift coefficients are repulsive and up to four times larger than the total drag coefficients. During overtaking manoeuvres, increasing the relative speed of the overtaking ellipse predominantly affects the forces on the overtaken ellipse. The mean drag force on the overtaken ellipse increases with increasing speed difference. Mean lift forces during the overtaking manoeuvre are repulsive for both bodies; as the speed difference increases, the repulsive force increases on the overtaken body and decreases on the overtaking body. Overall, these results highlight that the lateral forces in hydrodynamic interactions between bodies in formation dominate the hydrodynamic interactions. Further, the results indicate that future work is needed to investigate how viscous and three-dimensional effects change the lateral forces between side-by-side submerged bodies.

Impact Statement

The hydrodynamic forces and moments experienced by a pair of bodies in a free-stream flow can significantly differ from those acting on an isolated body. These hydrodynamic interactions, dependent on the relative positions and speeds of the bodies, can either enhance or impair operational performance metrics for underwater vehicles or biological swimmers. Existing research primarily concentrates on drag coefficient changes in stationary configurations. However, lateral forces and yawing moments are crucial as they determine the extent to which control systems need to intervene to maintain the bodies in their relative positions, leading to additional hydrodynamic drag overhead. These insights are even more important for overtaking manoeuvres. The findings of this study illustrate the significance of lateral forces on submerged bodies for side-by-side configurations and overtaking manoeuvres. Further, our work indicates the need for further research into viscous and three-dimensional effects on these lateral forces. Overall, the results improve our understanding of unmanned underwater vehicle formations and fish schooling dynamics.

1. Introduction

The hydrodynamic interactions between bodies moving in close formation within a fluid flow have been investigated from a variety of perspectives. The hydrodynamics of two unmanned underwater vehicles

(UUVs) operating in close formation have previously been modelled using three-dimensional (3-D) Reynolds-averaged Navier–Stokes (RANS) simulations and experimental testing, revealing that UUV interactions can be either beneficial or harmful to overall drag depending on the formation (Rattanasiri, Wilson & Phillips 2014; Tian *et al.* 2017; Zhang, Chao & Pan 2019*a*). Across these studies, echelon-like configurations were found to offer benefits for both UUVs together, with the drag decrease on the trailing body outweighing the drag increase on the leading body. Quantitative predictions on the drag reduction across these studies vary significantly, with maximum drag variations relative to an isolated body ranging from ±100 % (Rattanasiri *et al.* 2014) to +10 % and −30 % (Zhang *et al.* 2019*b*). In-line configurations find significant drag reductions for both UUVs as well, but in the absence of propeller wake modelling these results do not translate to realistic predictions. Formation drag reduction is also of interest in land-based applications such as cycling (Blocken *et al.* 2022) and car racing (Romberg, Chianese & Lajoie 1971).

Hydrodynamic interactions are prevalent in biological swimmers, where they are thought to reduce energy expenditure for one or multiple individuals in a formation. Dolphin and whale calves are hypothesized to exploit drag-advantaged swim formations (Noren & Edwards 2011; Shoele & Zhu 2015). By swimming in certain positions relative to its mother, the calf experiences a decrease in hydrodynamic drag, leading to a predicted reduction in swimming effort of as much as 90 % (Weihs 2004). A more complex setting is offered by fish swimming, where the hydrodynamic force interactions and benefits of schooling have been a long-standing debate in the scientific community (Weihs 1973; Partridge & Pitcher 1979). The additional complexity in fish schooling over UUVs is the active body deformation that leads to complex vortical wakes, and creates a dependency between the hydrodynamic benefits of formation patterns and phase differences in the swimming kinematics of the fish in the school (Li *et al.* 2020; Timm, Pandhare & Masoud 2023).

The cases mentioned above primarily consider the effects of the drag coefficient of bodies translating in various fixed formation patterns. From a practical perspective, however, the hydrodynamic lateral (sway) forces and (yaw) moments within a given formation pattern are important as well. For UUVs, active control of rudders or asymmetric thrust is required to maintain a formation, but this requires a suitable control mechanism and further comes at an additional energetic cost associated with induced drag. Similarly, for biological swimming any efforts at maintaining course and relative position will require additional muscular activations, coming at an energetic cost. It is thus important to quantify the lateral forces and yaw moment, relative to any changes in the hydrodynamic drag within a given formation.

Compared with the changes in drag force, there is significantly less existing research on the lateral forces and moments on a pair of submerged bodies moving together in a fluid flow, forcing a broader look at the existing results. An experimental study on equal-sized ellipsoidal bodies placed side by side showed that lateral forces reach up to 50 % of the total drag force (Molland & Utama 2002). More results are available for lateral forces in ship–ship interactions, typically investigated using potential flow techniques (Tuck & Newman 1976) or experimental analyses (Vantorre, Verzhbitskaya & Laforce 2002), and recently reviewed in Muscat-Fenech *et al.* (2022). Broadly, existing results state that lateral forces between two ships are attractive when the ships are moving side by side and repulsive when, roughly, the bow of one ship clears the stern of the other. These findings are qualitatively consistent with a potential flow study on submerged slender bodies of revolution (Wang 2007). Experiments found that lateral force magnitudes can be significantly larger than the drag force on the ships (Vantorre *et al.* 2002). In the context of flapping foils, Kurt & Moored (2018) used experiments at Reynolds numbers of $O(10^4)$ of tandem pitching wings to show that the mean lift coefficient can change from repulsive (in-phase motions) to attractive (out-of-phase) depending on the relative phase of the pitching motions between the two wings.

Besides equal speed interactions, the effect of relative motion on all force and moment coefficients is important when considering practical scenarios where overtaking manoeuvres would be necessary. With the bodies in relative motion, close-range hydrodynamic interactions will gain a dependency on the speed ratio between the two bodies. Within the ocean engineering community this has been predominantly investigated in potential flow settings, for submerged bodies (Wang 2007) and for ship

https://doi.org/10.1017/flo.2024.21 Published online by Cambridge University Press

overtaking manoeuvres (Skejic & Faltinsen 2007; Xiang & Faltinsen 2011; Yu, Wang & Yeung 2019), complemented by ship–ship interaction experiments (Vantorre *et al.* 2002; Muscat-Fenech *et al.* 2022). For low overtaking speeds, the hydrodynamic interactions agree roughly with the forces found for interactions without relative motion. The model test results in Vantorre *et al.* (2002) do show significant dependency on the results for lateral forces depending on the ship types used in the experiments. Larger overtaking speeds generally amplify the trends, with the larger response to the velocity difference occurring on the slower, overtaken body, rather than the faster, overtaking body (Vantorre *et al.* 2002; Wang 2007).

From the results above, there is a lack of quantitative, high-fidelity analysis of the lateral forces on side-by-side submerged bodies without and with relative motions. Existing knowledge is predominantly concentrated around potential and very high Reynolds number flows, mostly for ships, which only provides limited insight into the fully submerged setting relevant for smaller-scale UUVs (Mintchev *et al.* 2014; Hackbarth, Kreuzer & Solowjow 2015), biological swimmers and relative motions in a formation. Simultaneously, the interaction between heaving and/or pitching fins is predominantly investigated at lower Reynolds numbers, but involves significantly more complexity with respect to the vortical wakes induced by the relative lateral and angular kinematics of the fins. Consequently, the base problem of two bluff bodies moving side by side in a viscous incoming flow without and with relative motion provides an open area of study, especially when considering the lateral forces and moments.

Here, we use 2-D numerical simulations to characterize the hydrodynamic interactions between 6 : 1 (length-to-width) ellipses for different configurations and relative speeds. The ellipse interactions were studied using high-fidelity simulations of an incompressible, viscous flow with chord-based Reynolds numbers $1500 \leq Re \leq 3000$. These Reynolds numbers are similar to many studies on biological interactions although much lower than many engineering applications of underwater vehicles. However, as argued above, studying the lower end of the Reynolds number range provides complementary insights into viscous and transient effects while offering high-fidelity numerical results. Further, tackling a 2-D problem offers more flexibility in exploring a wide parameter space, and complements existing results on hydrodynamic interactions between cylinders (Sumner 2010) and foils and swimmers (e.g. Dewey *et al.* 2014; Kelly *et al.* 2023; Timm *et al.* 2023) that extend into this Reynolds number regime.

The rest of this work is structured as follows. Section 2 explains the computational method and numerical parameters. Section 3 briefly states the drag coefficient found for isolated elliptical bodies across the Reynolds number regime considered here, which serves as reference to quantify the hydrodynamic interactions of ellipse pairs. The main results are presented and discussed in § 4 for two ellipses operating at the same speed, and § 5 for overtaking manoeuvres. Finally, § 6 describes the conclusions of this work.

2. Methodology and set-up

In this section, we briefly explain the details of the numerical methodology, including physical parameters and definitions used in the simulations.

2.1. Simulation methodology

All simulations in this work are performed with a direct numerical solver for the 2-D incompressible Navier–Stokes equations. We solve the equations in a conservative vorticity–velocity form

$$\frac{\partial \omega}{\partial t} + \boldsymbol{\nabla} \cdot (\boldsymbol{u}\omega - \nu \boldsymbol{\nabla}\omega) = 0, \tag{2.1}$$

with $\omega = \boldsymbol{\nabla} \times \boldsymbol{u}$ the scalar vorticity field, $\boldsymbol{u}$ the velocity field and ν the kinematic viscosity. With ω as primary variable, the velocity field can be recovered by solving a scalar Poisson equation

$$\nabla^2 \psi = -\omega, \tag{2.2}$$

https://doi.org/10.1017/flo.2024.21 Published online by Cambridge University Press

where ψ is the streamfunction so that $\boldsymbol{u} = \boldsymbol{\nabla}\times\psi + \boldsymbol{U}_\infty$, with $\boldsymbol{U}_\infty$ any irrotational, divergence-free velocity field that satisfies the far-field boundary conditions.

Our solver discretizes these equations on a uniform Cartesian grid organized in constant-size blocks of $N_b \times N_b$ grid points where, in this work, $N_b = 32$ grid points. The advection term on the left-hand side is discretized using a third-order conservative upwind finite-difference scheme (Shu 1998), and the diffusion term uses a second-order centred finite-difference scheme. The Poisson equation is solved using a fast Fourier transform library (Caprace, Gillis & Chatelain 2021) with arbitrary combinations of free-space, periodic or symmetry/mirror boundary conditions on the domain boundaries. Finally, we use a third-order low-storage Runge–Kutta scheme for time integration, imposing a Courant–Friedrichs–Lewy-based stability constraint.

The no-slip boundary conditions on the immersed body(-ies) are enforced to second-order accuracy using an immersed interface method (IIM). As an embedded geometry technique, the IIM removes the need for meshes to conform to the boundary geometry, which enables the type of relative motions for side-by-side bodies presented below. Our version of the IIM imposes boundary conditions using a polynomial extrapolation of the field across immersed boundaries, taking into account any body boundary conditions, and using the extrapolated values in a standard free-space finite-difference scheme. This approach essentially injects local corrections in the finite-difference stencil to account for the presence of the boundary. We combine this approach with a low-rank correction approach to enforce a no-through boundary condition on the velocity field when solving from the vorticity. Further, the dynamic evolution of vorticity is augmented with a Thom-like wall-vorticity boundary condition which enforces the no-slip condition through the diffusion of the wall-bounded vortex layer into the flow (Thom 1933; Gillis *et al.* 2019). The approach is described and validated for single and multiple stationary bodies in Gabbard *et al.* (2022), and single and multiple moving bodies in Ji, Gabbard & van Rees (2023).

Throughout this study, we choose a simulation area as though viewed from above, with the positive x-axis pointing to the right, the positive y-axis pointing upward and the positive z-axis pointing out of the page and toward the viewer. In all results below, we choose our computational frame of reference to follow the ellipse that is initially located upstream. Consequently, the left, top and bottom of the domain were treated as free-space boundaries, with no imposed restriction on the velocity or velocity gradient – instead, the velocity is solved so that it decays towards U_∞ far away from the body (Gabbard *et al.* 2022). The right domain boundary was treated as an outflow condition (Chatelain *et al.* 2013; Gabbard *et al.* 2022). For all simulations in this work, the density of the fluid is constant and free-surface effects are ignored as the bodies are assumed to operate at large depth.

2.2. Physical set-up and notation

Throughout this study, we fix the aspect ratio of the ellipses as $L/D = 6$, with L the ellipse length and D its height. This ratio is chosen because it is representative of many UUV aspect ratios and thus commonly used in biological and UUV studies featuring elliptical (2-D) and ellipsoidal (3-D) shapes.

We study configurations of two ellipses in a free-space domain. We define ellipse 0 as the initially upstream ellipse and ellipse 1 as the initially downstream ellipse (figure 1). During the overtaking simulations, ellipse 1 moves in the negative x-direction to overtake ellipse 0. Denoting the centroid position of ellipse 0 as (x_0, y_0) and of ellipse 1 as (x_1, y_1), we define the non-dimensional quantities $x^* = (x_0 - x_1)/L$ and $y^* = (y_0 - y_1)/L$ to denote the relative positions between the two. During overtaking manoeuvres, x^* increases from its initial negative value (ellipse 1 downstream of ellipse 0) to its final positive value (ellipse 1 upstream of ellipse 0). Throughout this work y^* remains a constant positive value set independently for each simulation.

During overtaking, we introduce relative motion between the two ellipses. Here, for simplicity, we define $U_0 > 0$ and $U_1 > 0$ as the speeds of ellipses 0 and 1, respectively. As noted before, the simulations are performed in a frame of reference moving with ellipse 0 by introducing a left-to-right background flow velocity u_∞ with magnitude $u_\infty = U_0$. In this frame, the x-component of the velocity of ellipse 0 is $u_0 = 0$ and this quantity for ellipse 1 is $u_1 = U_0 - U_1$. However, our results below will be discussed

https://doi.org/10.1017/flo.2024.21 Published online by Cambridge University Press

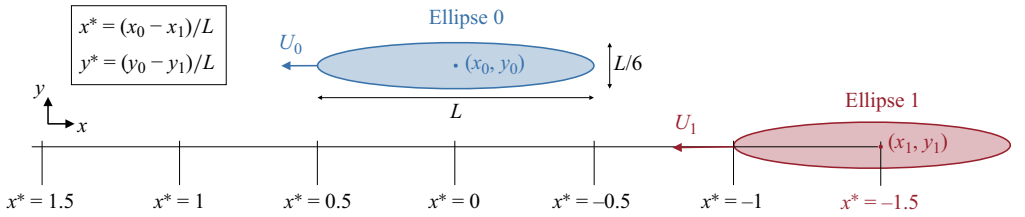

Figure 1. *Set-up and notation for the ellipse simulations, with the drawn state corresponding to* $x^* = -1.5$ *and* $y^* = 0.3$.

only with reference to the positive ellipse speeds U_0 and U_1, and the associated length-based Reynolds numbers

$$Re_0 = \frac{U_0 L}{\nu}, \quad Re_1 = \frac{U_1 L}{\nu}. \tag{2.3a,b}$$

The hydrodynamic quantities of interest in this study are the non-dimensional force and moment coefficients. Specifically, we define the drag, lift and moment coefficient for each ellipse as

$$\left.\begin{aligned} C_{D,0}(t) &= \frac{F_{x,0}(t)}{\frac{1}{2}\rho U_0^2 L} \quad C_{D,1}(t) = \frac{F_{x,1}(t)}{\frac{1}{2}\rho U_1^2 L} \\ C_{L,0}(t) &= \frac{F_{y,0}(t)}{\frac{1}{2}\rho U_0^2 L} \quad C_{L,1}(t) = -\frac{F_{y,1}(t)}{\frac{1}{2}\rho U_1^2 L} \\ C_{M,0}(t) &= -\frac{M_{z,0}(t)}{\frac{1}{2}\rho U_0^2 L^2} \quad C_{M,1}(t) = \frac{M_{z,1}(t)}{\frac{1}{2}\rho U_1^2 L^2} \end{aligned}\right\}, \tag{2.4}$$

with $F_{(x,y)}$ the forces in the (x, y) direction and M_z the yaw moment around the centroid of the ellipse, positive counter-clockwise. We emphasize the normalization with U_0 and U_1 for ellipse 0 and ellipse 1, respectively, as well as the opposing signs of C_L and C_M: the latter, together with the fact that $y_0 \geq y_1$ throughout, implies:

- a positive lift coefficient for either ellipse means the force points away from the other ellipse, i.e. a repulsive force; similarly a negative lift coefficient means the force points towards the other ellipse, i.e. an attractive force;
- a positive moment coefficient for either ellipse means a bow-out moment orientation; a negative moment coefficient means a bow-in moment orientation.

This choice is consistently made throughout the plots below to simplify the interpretation of the results.

These quantities depend on time, and in this study we have normalized time t by the convective time scale as

$$t^* = tU/L. \tag{2.5}$$

We further define time-averaged force and moment coefficients, defined for each quantity in (2.4), as

$$\bar{C}_F = \frac{1}{t_f - t_s} \int_{t_s}^{t_f} C_F(t)\, \mathrm{d}t, \tag{2.6}$$

with t_s and t_f the start and end of the averaging window specified in the results sections below.

https://doi.org/10.1017/flo.2024.21 Published online by Cambridge University Press

2.3. Numerical set-up

2.3.1. Initial transient

After starting each simulation, the wake behind the ellipses remains symmetric for a long time as the absence of sufficient numerical noise suppresses the vortex shedding instability. To accelerate the onset of shedding, we impose an early-time transient lateral perturbation in the free-stream velocity for all simulations discussed below. The perturbation consists of a temporary, smoothly increasing and decreasing addition of a flow in the lateral y-direction, described through the function

$$f(t) = \mathrm{e}^{-t^2/(1-t^2)}. \tag{2.7}$$

This function is shifted and scaled so that the lateral component to the free-stream velocity activates at $t^* = 1$, peaks at $t^* = 2$ and vanishes again at $t^* = 3$, with a peak amplitude of u_∞.

2.3.2. Domain size study

The upstream, top and bottom edges of our domain are free-space boundaries. Their distances from the body are solely set by the requirement to contain the vortical wake. Preliminary work found that a distance of $0.83L$ in front of the upstream ellipse, and a total domain height equal to half the total domain length, are sufficient choices to capture the vorticity field.

The downstream edge, however, is an outflow boundary condition. In previous work (Gabbard *et al.* 2022), we found that positioning the outflow boundary approximately 30 diameters behind a cylinder gives converged results for that flow. Here, we investigate the required distance for our ellipse configuration. To do so, we study a single ellipse and fix the resolution to $L/h = 175$. The distance from the trailing ellipse to the outflow boundary L_{out} is expressed relative to L and varied as $L_{out}/L \in [3, 5, 7, 8, 9, 11, 13]$. We set the Reynolds number to the highest value used in this work so that $Re = UL/\nu = 3000$, advance the flow until $t^* = 67$ and compute for each domain size the mean drag on the ellipse between $t^* = 40$ and $t^* = 60$. Comparing the mean drag with the value at $L_{out}/L = 13$, we find that choosing $L_{out}/L \geq 8$ keeps the difference within 1 % of the longest domain result. For the remainder of this study, we therefore ensure all our simulation domains are set up so that $L_{out}/L \geq 8$, where L_{out} measures the initial distance from the most downstream ellipse to the outflow boundary.

2.3.3. Grid resolution study

To determine the spatial resolution required for accurate simulation results, we perform a number of simulations at varying resolutions for both a single ellipse and a pair of ellipses. The studies are performed at the maximum considered Reynolds number $Re = 3000$ and, for the pair of ellipses, at the minimum considered centre-to-centre distance of $0.3L$. We run the simulations until final times $t^* = 67$ (single ellipse) and $t^* = 100$ (two ellipses) and normalize the grid spacing h with L, so that L/h describes the number of grid points along the length of an ellipse. For all cases, we position the ellipses so that the distance from their trailing edge to the outflow boundary is $8L$, in accordance with the domain study results described above.

For a single ellipse, we consider resolutions $L/h \in [100, 150, 175, 200, 250]$ and record the mean drag coefficient from $t^* = 40$ to $t^* = 60$ for each resolution. Our results are shown in the second and third columns of table 1, where we report both the mean drag coefficient and the relative difference at any resolution compared with the finest grid results at $L/h = 250$. The results show that a resolution above $L/h = 150$ is sufficient to obtain a mean drag value to within 1 %–2 % of the finest resolution result.

For the ellipse pair, we consider $L/h \in [150, 175, 200, 250]$, so that the minimum number of grid points across the gap ranges from 20 to 33. We report the average mean drag and average mean lift coefficient for the ellipse pair, as well as the percentage difference in these quantities from the finest resolution result at $L/h = 250$. The lift coefficient is somewhat slower to converge but still a resolution of $L/h = 175$ is sufficient to find a difference under 5 % with respect to the finest grid result.

We note that these simulations are run at the highest Reynolds number and, for the two ellipse case, at the closest overall distance between the bodies, and thus provide the most challenging flow

https://doi.org/10.1017/flo.2024.21 Published online by Cambridge University Press

Table 1. *Resolution study for simulations with a single ellipse (columns 2 and 3), as well as simulations with two side-by-side ellipses with $y^* = 0.3$ (columns 4 through 7). All differences are computed with respect to the finest resolution result $L/h = 250$.*

	Single ellipse		Side-by-side ellipses			
L/h	$\bar{C}_{D,iso}$	$\Delta\bar{C}_{D,iso}$ (%)	$(\bar{C}_{D,0} + \bar{C}_{D,1})/2$	$\Delta\bar{C}_D$ (%)	$(\bar{C}_{L,0} + \bar{C}_{L,1})/2$	$\Delta\bar{C}_L$
100	0.1025	13.2				
150	0.0927	2.35	0.1131	0.07	−0.3422	5.65
175	0.0915	1.00	0.1121	−0.75	−0.3371	4.07
200	0.0911	0.53	0.1125	−0.49	−0.3296	1.76
250	0.906	—	0.1130	—	−0.3239	—

Table 2. *Time-averaged drag coefficients of an isolated ellipse in a free stream at the different Reynolds numbers considered in this work.*

Re	1500	1875	2250	2625	3000
$\bar{C}_{D,iso}$	0.1171	0.1067	0.1005	0.0958	0.0918

configuration. With this in mind, we consider $L/h = 175$ as a sufficient resolution to proceed and use this resolution for all simulation results presented below, unless specified otherwise.

3. Drag of isolated ellipse at various speeds

To provide a reference for all results below, we simulated the time-averaged drag coefficient of an isolated ellipse in a free stream at different Reynolds numbers. These simulations were done with $L/h = 175$, $L_{out}/L = 9$ and drag coefficients are averaged between $t^* = 40$ and $t^* = 60$. Table 2 shows the results of $\bar{C}_{D,iso}$ at the Reynolds numbers considered in this work, $Re = 1500$, 1875, 2250, 2625 and 3000, showing a slight decay consistent with the drag on bluff bodies in this Reynolds number regime (Wieselsberger 1921).

For all results below, these drag coefficient values on isolated ellipses will be used as reference to quantify the effect of hydrodynamic interactions between an ellipse pair.

4. Flow past ellipses without relative motion

To provide a reference for the overtaking cases, we investigate first the case of flow past two ellipses without relative motion. To do so, we fix $Re_0 = Re_1 = 1500$ and vary $0 \le x^* \le 1.5$ and $0.3 \le y^* \le 0.6$ in increments of $1/6$ and $1/10$, respectively. For each pair (x^*, y^*) we run a simulation to steady state and record the time-averaged coefficients for drag, lift and moment. Using the intrinsic symmetry in the problem, we use the results from this quadrant to report the forces on both ellipses for the entire range $-1.5 \le x^* \le 1.5$. As reported above, at this Reynolds number, the mean drag coefficient on an isolated ellipse is $\bar{C}_{D,iso} = 0.1171$, and both the mean lift coefficient $\bar{C}_{L,iso}$ and the mean moment coefficient $\bar{C}_{M,iso}$ are zero.

4.1. Results

Figure 2 shows the results of the force coefficients on ellipse 0 as a function of (x^*, y^*), i.e. the relative location of ellipse 1, in a set of contour plots. As the results are symmetric with respect to the sign of y^*, each contour plot shows a different quantity in the top and bottom halves. The top-left contour

https://doi.org/10.1017/flo.2024.21 Published online by Cambridge University Press

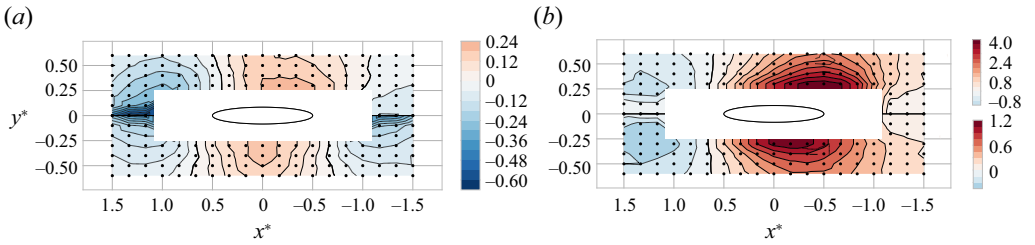

Figure 2. *Contour plot of drag force coefficient changes (left) and lift force/moment coefficient (right) on ellipse 0 travelling right to left (Re = 1500) as a function of the relative location of ellipse 1 travelling at the same speed. On the left, the top half contour levels indicate $C_{D,0}/C_{D,iso} - 1$, whereas the bottom half contour levels indicate $(C_{D,0} + C_{D,1})/(2C_{D,iso}) - 1$. On the right, the top half of the plot shows $C_{L,0}/C_{D,iso}$ and the bottom half shows $C_{M,0}/C_{D,iso}$, where the lift coefficient is defined positive when repulsive, and negative when attractive; similarly, the moment coefficient is defined positive for bow-out and negative for bow-in. In all plots, the zero contour is indicated with a solid black line, and the simulated data points by solid black circles.*

plot shows a relative drag coefficient of $\bar{C}_{D,0}/\bar{C}_{D,iso} - 1$, whereas the bottom-left contour plot shows the relative average drag coefficient $(\bar{C}_{D,0} + \bar{C}_{D,1})/(2\bar{C}_{D,iso}) - 1$. The right contour plot shows $\bar{C}_{L,0}/\bar{C}_{D,iso}$ in the top half, and $\bar{C}_{M,0}/\bar{C}_{D,iso}$ in the bottom.

The behaviour of the drag coefficient shows that, generally, a side-by-side configuration is equally disadvantageous for both ellipses, with a drag coefficient increase of around 24 % for the closest lateral separation of $y^* = 0.3$, decaying to 5 %–10 % for $y^* = 0.6$, depending on the precise value of x^*. Staggered configurations reduce the drag only for the trailing ellipse when $0.5 < |x^*| < 1.0$, and for both ellipses when $|x^*| > 1.0$ – although disproportionately so for the trailing ellipse. A completely in-line configuration leads to up to 60 % drag decrease of the trailing ellipse, and approximately 5 % for the leading ellipse. Taken together, the average drag of both ellipses decreases compared with an isolated ellipse for $|x^*| > 0.6$.

The lift coefficient (top-right in figure 2) shows the lift coefficient on ellipse 0 as repulsive for $x^* < 0.6$, i.e. for configurations where the second ellipse is slightly in front, side by side and aft of ellipse 0. Only for $x^* > 0.6$, i.e. a staggered configuration where the second ellipse is further in front of ellipse 0, does the nature of the lift coefficient on ellipse 0 change to attractive. The behaviour of the moment coefficient follows largely that of the lift coefficient. The lift and moment coefficients are normalized with $\bar{C}_{D,iso}$ to demonstrate that, by far, these effects dominate those observed on drag. Specifically, the peak mean repulsive lift coefficient is approximately four times $\bar{C}_{D,iso}$ for the closest lateral separation distance $y^* = 0.3$. With our normalization, any moment coefficient $\bar{C}_M$ is statically equivalent to a force couple of the same value applied to the front and aft of the ellipse. From figure 2, we observe that this force couple reaches values comparable to $\bar{C}_{D,iso}$. These big changes in $\bar{C}_L$ and $\bar{C}_M$, from their zero values for an isolated ellipse, dominate compared with the changes in $\bar{C}_D$ for both ellipses. From a practical perspective, this means that the manoeuvring cost of maintaining a given vehicle formation will be important. Consequently, any analysis of changes in drag coefficients between different configuration is incomplete when that cost is not taken into account.

4.2. Discussion

A significant body of work exists on the flow-mediated interactions between two 2-D cylinders placed in various configurations, and the related effects on the drag, lift and moment coefficients (Hori 1959; Zdravkovich 1977; Sumner 2010). Notably, these studies find reduced drag for in-line configurations and mean average drag increases for side-by-side configurations, similar to our work. Further, they find repulsive lift coefficients in side-by-side configurations, and slight attractive lift forces for narrow staggered arrangements. These features are common to our results as well. The Reynolds number effect

https://doi.org/10.1017/flo.2024.21 Published online by Cambridge University Press

on these qualitative regimes seems to be relatively small, and our qualitative results at $Re = 1500$ match well those at Reynolds numbers ten or a hundred times larger. Available results on side-by-side spheres (all in the Reynolds number range $50 \leq Re \leq 300$) also show a repulsive lift force for the separation distances considered here (Kim, Elghobashi & Sirignano 1993; Brydon & Thompson 2001; Yoon & Yang 2007). Further, the experimental results of Kurt & Moored (2018) show that, for in-phase pitching motions, a pair of tandem wings also experiences a net repulsive lift force.

Comparing with UUV results, the drag interactions observed in this study also qualitatively resembled those in Rattanasiri *et al.* (2014) and Tian *et al.* (2017), who characterized drag interactions between twin prolate spheroids at $Re = O(10^6)$ using RANS simulations. A notable exception was that the push region identified by Rattanasiri *et al.* (2014) in the closest tandem configuration of $(x^*, y^*) = (-1.17, 0.0)$ was not observed in the results of this study. Apart from the large difference in Reynolds number (which did not otherwise affect the drag interaction regions significantly), the lack of a push region could be attributed to limitations in the chosen grid resolution between ellipses at the closest spacing, or a small difference in the flow characteristics of two dimensions versus three dimensions at this location. However, the inconsistency at this configuration is not particularly relevant to the UUV application because neither simulation accounts for propeller effects, which are expected to make a sizable difference in the flow characteristics when one UUV is positioned in the wake of the other.

In contrast to the largely matching trends in drag coefficients, our results on the lateral forces are very different compared with UUV results. In particular, several 3-D RANS-based studies at Reynolds numbers of $O(10^6)$ show an attractive lift force between side-by-side ellipsoids and similar streamlined bodies, compared with the repulsive lift force reported in this work. Specifically, we believe that Romberg *et al.* (1971), Molland & Utama (2002), Leong *et al.* (2015), Yuan *et al.* (2015) and Zhang *et al.* (2019*a*) all report attractive lift forces across various scenarios for side-by-side bodies of either equal or different sizes in three dimensions at high Reynolds numbers. This points towards Reynolds number, geometry and/or three-dimensionality effects on the sign of the lift coefficient between side-by-side bodies. Physically, these parameters could all affect pressure gradients on the inside of the gap, and thus the flow acceleration and boundary layer separation location. Other important factors that merit further investigation include blockage in both numerical and experimental settings, and the choice of turbulence model in RANS simulations which is known to affect results on comparable geometries in complex flow conditions (Kim, Rhee & Miller 2013).

5. Flow past ellipses during an overtaking manoeuvre

For the overtaking manoeuvres, ellipse 0 moves at a constant speed associated with $Re_0 = 1500$, and ellipse 1 overtakes ellipse 0 at a constant speed. The overtaking manoeuvre of ellipse 1 is defined in terms of the time-varying speed

$$\tilde{U}_1(t) = \begin{cases} U_0 & t < t_0, \\ U_0 + \dfrac{1}{2}\left(1 - \cos\left(\pi \dfrac{t - t_0}{t_1 - t_0}\right)\right)(U_1 - U_0) & t_0 \leq t \leq t_1, \\ U_1 & t > t_1. \end{cases} \tag{5.1}$$

The initial window $t < t_0$ where ellipse 1 moves at the same speed as U_0 ensures that the wake is developed prior to the start of the relative motion, whereas the transition phase from t_0 to t_1 is designed to smoothly change the velocity between U_0 and U_1. Here, we set $t_0^* = 16.7$ and $t_1^* = 19.2$.

In all overtaking simulations, we ensure that the time at which ellipse 1 reaches its U_1 speed coincides with a relative distance of $x^*(t_1) = -1.5$, so that we can gather data in the range $-1.5 \leq x^* \leq 1.5$. This is achieved by integrating equation (5.1) in time to compute the distance travelled by ellipse 1 at t_1, and then initializing $x^*(0)$ so that $x^*(t_1) = -1.5$.

We vary the relative speed of ellipse 1 in the range $1.25 \leq U_1/U_0 \leq 2$, associated with Reynolds numbers in the range $1875 \leq Re_1 \leq 3000$. For each relative speed, we further vary the non-dimensional

https://doi.org/10.1017/flo.2024.21 Published online by Cambridge University Press

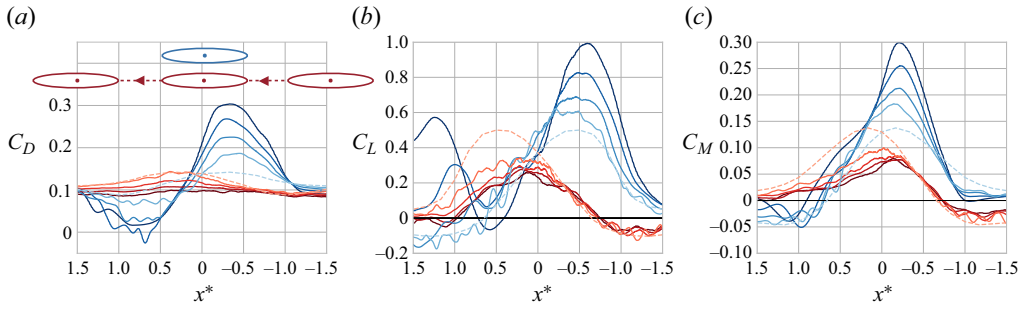

Figure 3. *Evolution of the drag (a), lift (b) and moment (c) coefficients on ellipse 0 (blue) and ellipse 1 (red) as a function of the non-dimensional separation distance x^*, with time progressing from right to left as indicated by the inset on the top left. The lateral separation distance is fixed at $y^* = 0.3$. For both ellipses, the lift coefficient is defined positive when repulsive, and negative when attractive; similarly, the moment coefficient is defined positive for bow-out and negative for bow-in. The line colour darkness increases with the Reynolds number of ellipse 1: $Re_1 \in [1875, 2250, 2625, 3000]$, and the case $Re_1 = Re_0 = 1500$ is indicated with a light-coloured dashed line.*

lateral separation distance $0.3 \leq y^* \leq 0.6$. We include also the results of the case with no relative motion ($Re_1 = Re_0 = 1500$) discussed in the previous section, by concatenating the time-averaged force/moment coefficient results at each value of x^* into an array, and interpreting the array as if x^* were equivalent to time. In this way, the case without relative motion can be interpreted as an overtaking simulation in the limit of $U_1/U_0 \to 1$.

5.1. Time-varying results

Figure 3 shows how the drag, lift and moment coefficients change as a function of the non-dimensional separation distance x^*. The plot shows results at the smallest separation distance $y^* = 0.3$ and all relative velocities $1.25 \leq U_1/U_0 \leq 2$. Further, we superimpose the integrated results from the previous section as a quasi-static approximation of the limit $U_1/U_0 \to 1$. Similar plots for other values of y^* are included in the Appendix.

Starting with the drag, we observe that, at low velocity ratios, the drag of the overtaking ellipse 1 (in red) increases as it approaches ellipse 0, similar to the steady-state results of the previous section. This trend decreases, however, as the velocity ratio increases, and at $U_1/U_0 = 2$ the drag of ellipse 1 even decreases compared with its isolated value when $x^* < 0$. Across all cases shown in figure 3, the peak drag on ellipse 1 is achieved when $0 \leq x^* \leq 0.5$, with the drag coefficients increasing by up to 35 % compared with their values in isolation. At $x^* = 1.0$, when ellipse 1 has cleared ellipse 0, the drag of ellipse 1 across all relative velocities has returned to within 10 % of the respective values in isolation. The trend for the overtaken ellipse 0, even though it is always moving at $Re = 1500$, is very different. As ellipse 1 approaches, ellipse 0 sees a significant increase in its drag coefficient, with a more pronounced trend for larger velocities of ellipse 1. The highest drag on ellipse 0 is achieved for $U_1/U_0 = 2$, when the separation distance $x^* = -0.35$, and reaches up to 2.5 times the isolated drag. As ellipse 1 passes, the trend reverses and ellipse 0 gains a large drag decrease, even gaining a net thrust for the largest velocity ratios around $x^* = 0.6$. As ellipse 1 moves ahead of ellipse 0, the drag on ellipse 0 increases again to roughly its isolated value.

The effect of U_1/U_0 on the lift and moment curves are very similar to the drag: for ellipse 1, an increase in U_1/U_0 diminishes the deviations from the quasi-static trends (dashed line), whereas for ellipse 0, an increase the overtaking velocity enhances the deviations from the quasi-static trends. The lift coefficients start out attractive for the upstream ellipse 0 and repulsive for the overtaking ellipse 1, changing to repulsive for both in the range $-0.5 \leq x^* \leq 0.7$, and then switching to attractive for ellipse 1

https://doi.org/10.1017/flo.2024.21 Published online by Cambridge University Press

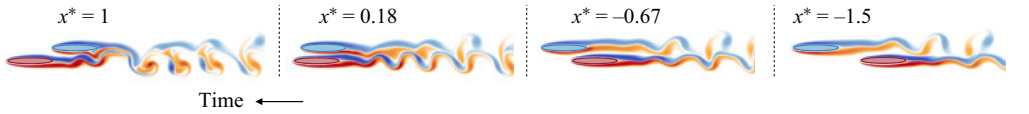

Figure 4. *Vorticity field at four instances during an overtaking manoeuvre with $U_1/U_0 = 2$ and $y^* = 0.3$. Time proceeds from right to left as ellipse 1 (in red) overtakes ellipse 0 (in blue).*

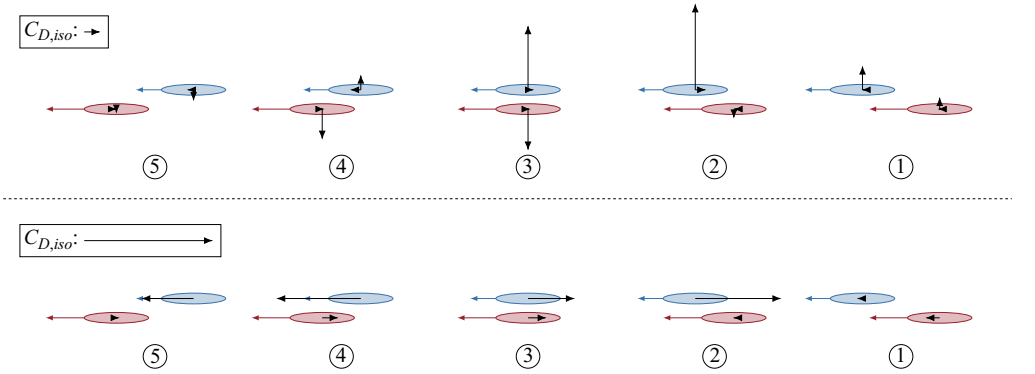

Figure 5. *Changes in drag and lift forces (a) and only drag (b) on the slower ellipse 0 (blue) and the overtaking ellipse 1 (red) during the overtaking manoeuvre (time increases from right to left), at $y^* = 0.3$ and $U_1/U_0 = 1.5$. The force arrows are scaled relative to the drag of an isolated ellipse at the speed of the slower ellipse, with a unit-length vector shown in the top-left rectangle. For the drag (bottom), the scale is increased to better see the relative effects. The forces shown are the mean forces within five interaction regions defined as (from right to left): 1: $-1.5 \leq x^* \leq -0.9$; 2: $-0.9 \leq x^* \leq -0.3$; 3: $-0.3 \leq x^* \leq 0.3$; 4: $0.3 \leq x^* \leq 0.9$; 5: $0.9 \leq x^* \leq 1.5$.*

only. This is largely in line with the regimes shown in figure 2 for the stationary interactions. The moment coefficients behave analogously to the lift, again following figure 2. Across all three generalized force coefficients, when x^* exceeds values around 0.5, the curves become oscillatory, predominantly for ellipse 0. Figure 4 shows that this coincides with the unsteady vortices that developed in the wake of ellipse 1, which for x^* roughly larger than 0.5 begin to affect the forces measured on the ellipse 0.

For the specific case of $U_1/U_0 = 1.5$ and $y^* = 0.3$, figure 5 shows the changes in the force coefficients in a more intuitive sketch, which provides a sense of the qualitative interactions as well as the relative magnitude of the associated force changes. The top sketch confirms that the predominant effects are the lift coefficient changes, which are comparatively stronger on ellipse 0 than on ellipse 1. The bottom sketch shows in more depth the changes in drag coefficient only, demonstrating again that dominant effects occur on ellipse 0, specifically in regions 2 and 4 when ellipse 1 is diagonally behind and in front, respectively.

Summarizing, we can see that the signs for all force coefficients, as a function of x^*, largely follow the stationary interactions of figure 2 across all values of U_1/U_0. The main effect of U_1/U_0 is on the amplitude of the force coefficients: for the overtaken ellipse 0 the amplitudes increase as U_1 increases; for the overtaking ellipse 1 the amplitudes decrease as U_1 increases.

The variation of the transient force coefficients during overtaking across all various lateral separation distances y^* is shown in figure 7 in the Appendix. The trends discussed above for $y^* = 0.3$ remain also at larger values of y^*, although with less pronounced peak force values and variations as a function of both x^* and U_1/U_0.

5.2. Time-averaged results

For each combination of y^* and U_1/U_0, we can integrate the drag, lift and moment coefficients for each ellipse between $x^* = -1.5$ and $x^* = 1.5$. Dividing this integral by the elapsed time gives a time-averaged

https://doi.org/10.1017/flo.2024.21 Published online by Cambridge University Press

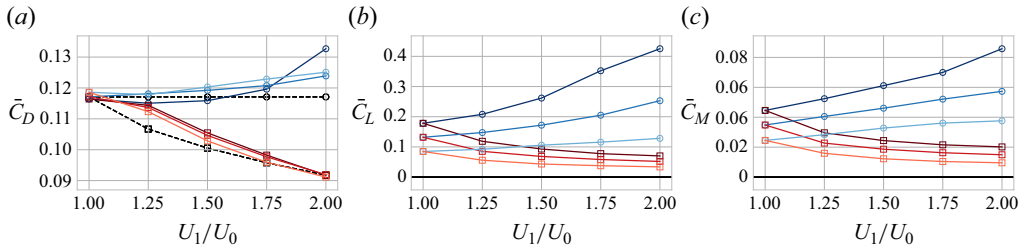

Figure 6. *Average drag (a), lift (b) and moment (c) coefficients on ellipse 0 (circles) and ellipse 1 (squares) during the overtaking manoeuvre, as a function of the velocity ratio U_1/U_0 ($Re_0 = 1500$ throughout). For both ellipses, the lift coefficient is defined positive when repulsive, and negative when attractive; similarly, the moment coefficient is defined positive for bow-out and negative for bow-in. The line colour lightness indicate the non-dimensional separation distance: $y^* \in [0.3, 0.4, 0.6]$ from darkest to lightest. For the drag coefficient, the black dashed lines indicate the drag coefficient of an isolated ellipse at each ellipse's Reynolds number.*

force coefficient, which for C_D specifically can be interpreted as an averaged power coefficient associated with the cost of the overtaking manoeuvre

$$\bar{C}_{P,i} = \frac{\dfrac{1}{t_e - t_s}\displaystyle\int_{t_s}^{t_e} F_{x,i}(t)\tilde{U}_i(t)\,\mathrm{d}t}{\dfrac{1}{2}\rho U_i^3 L} = \frac{\dfrac{1}{t_e - t_s}\displaystyle\int_{t_s}^{t_e} F_{x,i}(t)\,\mathrm{d}t}{\dfrac{1}{2}\rho U_i^2 L} = \bar{C}_{D,i}, \tag{5.2}$$

as long as $\tilde{U}_i(t) = U_i$ $(i = 0, 1)$ between t_s and t_e. Here, we choose the integration window such that $x^*(t_s) = -1.5$ and $x^*(t_e) = 1.5$, and both ellipses move at constant velocities during that time.

Figure 6 shows the average force and moment coefficient values as a function of the speed of the faster ellipse for the range of tested y^* values. In the plot of mean drag coefficient (left), we further plot the reference drag coefficient of an isolated ellipse $\bar{C}_{D,iso}$ at the Reynolds numbers of both ellipses associated with each U_1/U_0 with black dashed lines.

The mean force values confirm the trends observed in the transient results. The mean drag of ellipse 1 during the overtaking manoeuvre is only slightly increased compared with the value of an isolated ellipse at equivalent Reynolds number. Consequently, the mean drag is largely unaffected by the lateral separation distance. In contrast, the mean drag of ellipse 0 increases significantly as the overtaking speed of ellipse 1 increases, with a peak value of 0.133 or an approximately 13 % increase over the reference value at $y^* = 0.3$ and $U_1/U_0 = 2$. For $y^* > 0.3$ the increase appears monotonic with U_1/U_0, whereas for $y^* = 0.3$ the mean drag drops slightly below the reference value in the range $1 \leq U_1/U_0 \leq 1.5$. This might be related to the oscillations in the transient drag curve (figure 3, left), which we attribute to the effect of ellipse 1 on the dynamic vortex shedding of ellipse 0. This would imply a possible dependency of the precise transient drag evolution on the phase difference between the start of the overtaking motion and the vortex shedding cycle, likely more pronounced for smaller values of U_1/U_0. Overall, these results indicate that, during an overtaking manoeuvre between two bodies moving in the same direction, the average power required for the faster-moving overtaking body is largely unchanged from its value in free space. The slower-moving body, however, requires significantly more power to maintain its speed, and this cost increases with the speed difference of the overtaking body.

The mean lift coefficient of both ellipses is repulsive for all velocities and lateral distances. For ellipse 0, $\bar{C}_L$ increases with the velocity of ellipse 1, reaching $\bar{C}_L = -0.425$ at $y^* = 0.3$ and $U_1/U_0 = 2$, which amounts to 4.5 times the value of $\bar{C}_{D,iso}$ at this Reynolds number. The mean lift coefficient on the faster-moving ellipse 1 decreases with U_1/U_0, but still reaches values comparable to $\bar{C}_{D,iso}$ for $y^* = 0.3$ and $U_1/U_0 = 2$. Across all velocity ratios, increasing the lateral distance y^* decreases the magnitude of the mean lift coefficient for both ellipses.

https://doi.org/10.1017/flo.2024.21 Published online by Cambridge University Press

5.3. Discussion

Compared with a potential flow study on overtaking manoeuvres of submerged bodies (Wang 2007), our transient results in viscous flow differ substantially. In Wang (2007), the lift on the overtaking body is shown to be attractive first and then repulsive, consistent with our observations of ellipse 1; however, the overtaken body experiences an initial repulsion, then strong attraction when the bodies are side by side, followed by repulsion. Our results, in contrast, show that ellipse 0 experiences repulsion during the majority of the manoeuvre. As ellipse 1 pulls ahead, the lateral force on ellipse 0 drops and switches to attraction, at least for the small speed differences. We note that the trends of Wang (2007) match also potential flow (Yuan *et al.* 2015; Yu *et al.* 2019; Muscat-Fenech *et al.* 2022) and experimental (Vantorre *et al.* 2002) studies on ship–ship interactions, although free-surface and/or Reynolds number effects likely play a role in those results.

Our results further show a mean drag increase over the isolated drag coefficient for all separation distances $y^* > 0.3$, as well as mean repulsive lift coefficients. Increasing the velocity of the overtaking body (ellipse 1) decreases the changes in mean drag and lift on the overtaking body, while increasing the mean forces on the overtaken body (ellipse 0). This observation is consistent with a potential flow analysis of two slender bodies of revolution translating in proximity (Wang 2007) (§ 4.3 of that work), indicating that these trends can be expected across the entire Reynolds number regime.

6. Conclusions

In this work we characterize the hydrodynamic interactions due to the flow past two ellipses, focusing on drag and lift forces as a function of spatial configuration and relative motion.

In the absence of relative motion, we find that, depending on the longitudinal positions of the ellipses, the drag interaction is either mutually beneficial (drafting), detrimental (parallel), benefited the trailing ellipse (echelon) or did not produce a significant change on either ellipse (low interaction). The echelon configuration led to as much as a ∼20 % drag decrease for the downstream ellipse at the cost of a similar increase for the upstream ellipse. In most configurations, the lift force on both ellipses was repulsive with a significantly (up to four times) larger magnitude than the drag force, with the (bow-out) moment coefficient following a similar trend. In a practical application, this means that the lift will dominate the behaviour of the bodies, which has strong implications in terms of having to manoeuvre the ellipses to maintain their formation. All trends are repeated across the lateral separations tested, with the effect strengthening as the size of the gap between the ellipses reduces. Our results on drag and lift forces are qualitatively consistent with existing studies on cylinder–cylinder interactions at subcritical Reynolds numbers. Comparing with inviscid and high Reynolds number results of UUVs and ships, obtained from RANS simulations as well as potential flow analyses, we find similar trends in the drag coefficient. However, the lift coefficient in those results is predominantly attractive, which would imply a qualitative transition in the behaviour of the lift coefficient associated with viscous and/or 3-D effects.

During an overtaking manoeuvre with small speed ratios, the unsteady forces experienced by both ellipses qualitatively match the stationary results at each relative position. As the speed ratio increases, the changes in the mean drag, lift and moment coefficients on the overtaken ellipse increase significantly whereas the corresponding values on the overtaking ellipse diminish slightly, consistent with existing potential flow results. Within an overtaking manoeuvre we observe large variations in the drag and lift coefficients as a function of the relative longitudinal position. While located upstream of the overtaking ellipse, the overtaken ellipse experiences a peak drag increase of up to two-and-a-half times that of an isolated ellipse. This increase is matched by a similar drag decrease in the second half of the manoeuvre. The mean lift interaction between the ellipses is repulsive, with the slower ellipse experiencing a mean lift force up to two-and-a-half times the value under zero relative motion. Transient variations in lift coefficient on the overtaken ellipse increase with relative velocity and lateral proximity.

In general, the ellipses experience high lift and moment coefficients when operating in close proximity, with peak and mean values increasing during overtaking manoeuvres especially for the overtaken ellipse. These interactions tend to increase the difficulty of manoeuvring and need to be corrected by steering,

https://doi.org/10.1017/flo.2024.21 Published online by Cambridge University Press

which incurs additional drag forces that diminish any gains made from favourable configuration choices. In comparison with related studies in different flow regimes, we find that the magnitude and sign of the lift and moment coefficients are especially sensitive to variations in Reynolds number and geometry. Our results can be used for modelling these additional induced drag forces, while also pointing towards the need for future research on the sensitivity of the nature of lateral forces to Reynolds number and 3-D effects.

Declaration of interests. The authors declare no conflict of interest.

Funding. P.R. gratefully acknowledges funding from an MIT Mechanical Engineering Graduate Research Fellowship.

Appendix

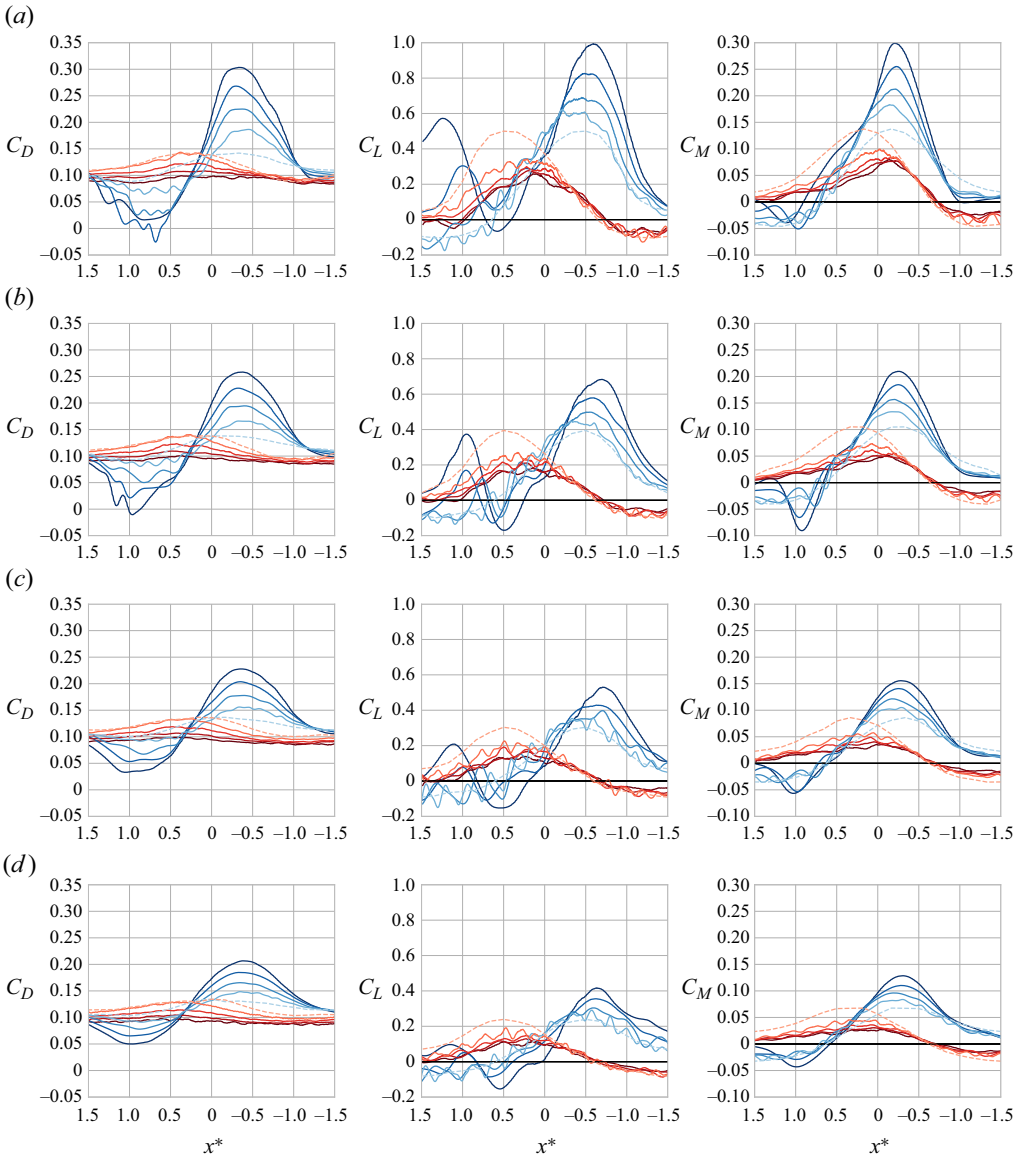

Figure 7. *Drag, lift and moment coefficient variations on ellipse 0 (blue) and ellipse 1 (red) as a function of x^* during the overtaking manoeuvre. (a–d): $y^* = 0.3$, $y^* = 0.4$, $y^* = 0.5$, $y^* = 0.6$. In each plot, for each ellipse, the line colour becomes darker as U_1/U_0 increases. See figure 3 for full caption.*

https://doi.org/10.1017/flo.2024.21 Published online by Cambridge University Press

References

Blocken, B., Defraeye, T., Koninckx, E., Carmeliet, J. & Hespel, P. 2022 CFD simulations of the aerodynamic drag of two drafting cyclists. *Comput. Fluids* **71**, 435–445.

Brydon, A. & Thompson, M. 2001 Flow interaction between two spheres at moderate Reynolds number. In *Proceedings of the 14th Australasian Fluid Mechanics Conference, Adelaide University, Adelaide, Australia* (ed. B. Dally), vol. 2 pp. 693–696. The University of Adelaide.

Caprace, D.-G., Gillis, T. & Chatelain, P. 2021 FLUPS: a Fourier-based library of unbounded Poisson solvers. *SIAM J. Sci. Comput*. **43** (1), C31–C60.

Chatelain, P., Backaert, S., Winckelmans, G. & Kern, S. 2013 Large eddy simulation of wind turbine wakes. *Flow Turbul. Combust*. **91** (3), 587–605.

Dewey, P.A., Quinn, D.B., Boschitsch, B.M. & Smits, A.J. 2014 Propulsive performance of unsteady tandem hydrofoils in a side-by-side configuration. *Phys. Fluids* **26** (4), 041903.

Gabbard, J., Gillis, T., Chatelain, P. & van Rees, W.M. 2022 An immersed interface method for the 2D vorticity-velocity Navier–Stokes equations with multiple bodies. *J. Comput. Phys*. **464**, 111339.

Gillis, T., Marichal, Y., Winckelmans, G. & Chatelain, P. 2019 A 2D immersed interface vortex particle-mesh method. *J. Comput. Phys*. **394**, 700–718.

Hackbarth, A., Kreuzer, E. & Solowjow, E. 2015 HippoCampus: a micro underwater vehicle for swarm applications. In *2015 IEEE/RSJ International Conference on Intelligent Robots and Systems (IROS)*. IEEE.

Hori, E. 1959 Experiments on flow around a pair of parallel circular cylinders. In *Proceedings of the 9th Japan National Congress for Applied Mechanics*, pp. 231–234.

Ji, X., Gabbard, J. & van Rees, W.M. 2023 A sharp immersed method for 2D flow-body interactions using the vorticity-velocity Navier–Stokes equations. *J. Comput. Phys*. **494**, 112513.

Kelly, J., Pan, Y., Menzer, A. & Dong, H. 2023 Hydrodynamics of body–body interactions in dense synchronous elongated fish schools. *Phys. Fluids* **35** (4), 041906.

Kim, I., Elghobashi, S. & Sirignano, W.A. 1993 Three-dimensional flow over two spheres placed side by side. *J. Fluid Mech*. **246**, 465–488.

Kim, S.-E., Rhee, B.J. & Miller, R.W. 2013 Anatomy of turbulent flow around DARPA SUBOFF body in a turning maneuver using high-fidelity RANS computations. *Intl Shipbuild. Prog*. **60** (1-4), 207–231.

Kurt, M. & Moored, K. 2018 Unsteady performance of finite-span pitching propulsors in side-by-side arrangements. In *2018 Fluid Dynamics Conference*. American Institute of Aeronautics and Astronautics.

Leong, Z.Q., Ranmuthugala, D., Penesis, I. & Nguyen, H. 2015 Quasi-static analysis of the hydrodynamic interaction effects on an autonomous underwater vehicle operating in proximity to a moving submarine. *Ocean Engng* **106**, 175–188.

Li, L., Nagy, M., Graving, J.M., Bak-Coleman, J., Xie, G. & Couzin, I.D. 2020 Vortex phase matching as a strategy for schooling in robots and in fish. *Nat. Commun*. **11** (1).

Mintchev, S., Donati, E., Marrazza, S. & Stefanini, C. 2014 Mechatronic design of a miniature underwater robot for swarm operations. In *2014 IEEE International Conference on Robotics and Automation (ICRA)*. IEEE.

Molland, A.F. & Utama, I.K.A.P. 2002 Experimental and numerical investigations into the drag characteristics of a pair of ellipsoids in close proximity. *Proc. Inst. Mech. Engrs* M *J. Engng Maritime Environ*. **216**, 107–115.

Muscat-Fenech, C.D., Sant, T., Zheku, V.V., Villa, D. & Martelli, M. 2022 A review of ship-to-ship interactions in calm waters. *J. Mar. Sci. Engng* **10**, 1856.

Noren, S.R. & Edwards, E.F. 2011 Infant position in mother-calf dolphin pairs: formation locomotion with hydrodynamic benefits. *Mar. Ecol. Prog. Ser*. **424**, 229–236.

Partridge, B.L. & Pitcher, T.J. 1979 Evidence against a hydrodynamic function for fish schools. *Nature* **279**, 418–419.

Rattanasiri, P., Wilson, P.A. & Phillips, A.B. 2014 Numerical investigation of a fleet of towed AUVs. *Ocean Engng* **80**, 25–35.

Romberg, G.F., Chianese, F. & Lajoie, R.G. 1971 Aerodynamics of race cars in drafting and passing situations. In *Society of Automotive Engineers Automotive Engineering Congress*, pp. 1–8.

Shoele, K. & Zhu, Q. 2015 Drafting mechanisms between a dolphin mother and calf. *J. Theor. Biol*. **382**, 363–377.

Shu, C.-W. 1998 Essentially non-oscillatory and weighted essentially non-oscillatory schemes for hyperbolic conservation laws. In *Advanced Numerical Approximation of Nonlinear Hyperbolic Equations*, pp. 325–432. Springer.

Skejic, R. & Faltinsen, O.M. 2007 A unified seakeeping and maneuvering analysis of two interacting ships. In *International Conference on Hydrodynamics*, pp. 209–218.

Sumner, D. 2010 Two circular cylinders in cross-flow: a review. *J. Fluids Struct*. **26**, 849–899.

Thom, A. 1933 The flow past circular cylinders at low speeds. *Proc. R. Soc. Lond. Ser.* A *Contain. Papers Math. Phys. Charact*. **141** (845), 651–669.

Tian, W., Mao, Z., Zhao, F. & Zhao, Z. 2017 Layout optimization of two autonomous underwater vehicles for drag reduction with a combined CFD and neural network method. *Complexity* **2017**, 1–15.

Timm, M.L., Pandhare, R.S. & Masoud, H. 2023 Multi-body hydrodynamic interactions in fish-like swimming. *Appl. Mech. Rev*. **76** (3), 030801.

Tuck, E.O. & Newman, J. 1976 Hydrodynamic interactions between ships. In *Proceedings of the 10th Symposium on Naval Hydrodynamics, Cambridge, MA, June 24–28, 1974*.

https://doi.org/10.1017/flo.2024.21 Published online by Cambridge University Press

Vantorre, M., Verzhbitskaya, E. & Laforce, E. 2002 Model test based formulations of ship-ship interaction forces. *Ship Technol. Res*. **49**, 124–141.

Wang, Q.X. 2007 An analytical solution for two slender bodies of revolution translating in very close proximity. *J. Fluid Mech*. **582**, 223–251.

Weihs, D. 1973 Hydromechanics of fish schooling. *Nature* **241**, 290–291.

Weihs, D. 2004 The hydrodynamics of dolphin drafting. *J. Biol*. **3**, 8.

Wieselsberger, C. 1921 Neuere feststellungen under die gesetze des flussigkeits und luftwiderstandes. *Phys. Z.* **22**, 321–328.

Xiang, X. & Faltinsen, O.M. 2011 Maneuvering of two interacting ships in calm water. *Mar. Syst. Ocean Technol.* **6** (2), 65–73.

Yoon, D.-H. & Yang, K.-S. 2007 Flow-induced forces on two nearby spheres. *Phys. Fluids* **19** (9), 098103.

Yu, D., Wang, L. & Yeung, R.W. 2019 Experimental and numerical study of ship-to-ship interactions in overtaking manoeuvres. *Proc. R. Soc.* A **475**, 1–23.

Yuan, Z., He, S., Kellett, P., Incecik, A., Turan, O. & Boulougouris, E. 2015 Ship-to-ship interaction during overtaking operation in shallow water. *J. Ship Res*. **59** (3), 172–187.

Zdravkovich, M.M. 1977 Review of flow interference between two circular cylinders in various arrangments. *Trans. Am. Soc. Mech. Engrs* **99**, 618–633.

Zhang, D., Chao, L. & Pan, G. 2019*a* Analysis of hydrodynamic interaction impacts on a two-AUV system. *Ships Offshore Struct*. **14** (1), 23–34.

Zhang, D., Pan, G., Shi, Y., Wang, P. & Chao, L. 2019*b* Investigation of the resistance characteristics of a multi-AUV system. *Appl. Ocean Res*. **89**, 59–70.

Cite this article: Rhodes P, van Rees WM (2024). Hydrodynamic forces on a side-by-side ellipse pair with and without relative motion. *Flow*, *4*, E27. doi:10.1017/flo.2024.21